CHEMISTRY
AN ASIAN JOURNAL

DOI: 10.1002/asia.200800065

Frontside versus Backside S_N2 Substitution at Group 14 Atoms: Origin of Reaction Barriers and Reasons for Their Absence

A. Patrícia Bento and F. Matthias Bickelhaupt*[a]

Abstract: We have theoretically studied the gas-phase nucleophilic substitution at group-14 atoms (S_N2@A) in the model reactions of $Cl^- + AH_3Cl$ (A = C, Si, Ge, Sn, and Pb) using relativistic density functional theory (DFT) at ZORA-OLYP/TZ2P. Firstly, we wish to explore and understand how the reaction coordinate ζ, and potential energy surfaces (PES) along ζ, vary as the center of nucleophilic attack changes from carbon to the heavier group-14 atoms. Secondly, a comparison between the more common backside reaction (S_N2-b) and the frontside pathway (S_N2-f) is performed. The S_N2-b reaction is found to have a central barrier for A = C, but none for the other group-14 atoms, A = Si–Pb. Relativistic effects destabilize reactant complexes and transition species by up to 10 kcal mol^{-1} (for S_N2-f@Pb), but they do not change relative heights of barriers. We also address the nature of the transformation in the frontside S_N2-f reactions in terms of turnstile rotation versus Berry-pseudorotation mechanism.

Keywords: activation strain model · density functional calculations · group 14 elements · nucleophilic substitution · reaction mechanisms

Introduction

Bimolecular nucleophilic substitution (S_N2) reactions play an important role in organic synthesis,[1] and various experimental and theoretical studies have therefore been devoted to obtain a better understanding of the nature of these processes.[2–8] The symmetric, thermoneutral S_N2 reaction between the chloride anion and chloromethane, $Cl^- + CH_3Cl$, in the gas phase is generally employed as the archetypal model for nucleophilic substitution [Eq. (1)].

$$Cl^- + H_3C{-}Cl \rightarrow Cl{-}CH_3 + Cl^- \quad (1)$$

This reaction proceeds preferentially through backside nucleophilic attack of the chloride anion at the carbon atom (S_N2@C) with concerted expulsion of the leaving group. A well-known feature of gas-phase S_N2@C reactions is their double-well potential energy surface (PES) along the reaction coordinate, shown in Figure 1. This PES is characterized by a central barrier, provided by a trigonal bipyramidal transition state (TS), that separates two pronounced minima, associated with the reactant and product ion-molecule complexes (RC and PC).

Interestingly, if one goes from the S_N2@C reaction of $Cl^- + CH_3Cl$ [Eq. (1)] to the corresponding S_N2@Si reaction of the isoelectronic and isostructural reaction system of $Cl^- + SiH_3Cl$ [Eq. (2)], the central barrier disappears.[6,9–11]

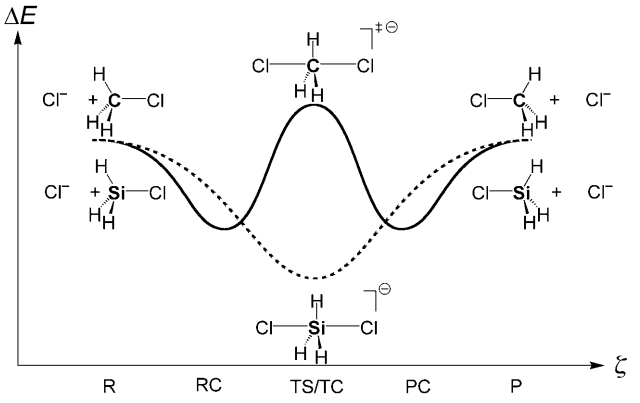

Figure 1. Potential energy surfaces for backside S_N2@C (plain) and S_N2@Si (dashed) reactions along the reaction coordinate ζ (R = reactants, RC = reactant complex, TS = transition state, TC = transition complex, PC = product complex, P = products).

[a] A. P. Bento, Dr. F. M. Bickelhaupt
Department of Theoretical Chemistry and
Amsterdam Center for Multiscale Modeling
Scheikundig Laboratorium der Vrije Universiteit
De Boelelaan 1083, 1081 HV Amsterdam (The Netherlands)
Fax: (+31) 20-598-7629
E-mail: FM.Bickelhaupt@few.vu.nl

Supporting information for this article is available on the WWW under http://dx.doi.org/10.1002/asia.200800065.

$$Cl^- + H_3Si{-}Cl \rightarrow Cl{-}SiH_3 + Cl^- \quad (2)$$

This phenomenon, which leads to a transition from a double-well to a single-well PES, is well-known (see Figure 1). Recently, we have shown in complementary studies that the disappearance of the central barrier in the S_N2@Si reactions is associated with less steric congestion around the large silicon atom as well as with a more favorable nucleophile-substrate interaction.[6–8] Interestingly, the central barrier reappears as the steric bulk around the silicon atom is raised, yielding the first example of an S_N2@Si reaction that proceeds by the classical double-well potential with a central reaction barrier. Importantly, these results also highlight the generally steric nature of the S_N2 barrier.

The available data are less abundant for pentacoordinate group-14 atoms heavier than silicon, that is, germanium (S_N2@Ge),[10,11] tin (S_N2@Sn),[10,12] and lead (S_N2@Pb).[12] They find that the central, pentacoordinate transition species is a stable intermediate in the case of germanium, tin, as well as lead. This suggests a single-well PES also for S_N2 at heavier group-14 atoms [Eqs. (3)–(5)].

Abstract in Portuguese: As reacções de substituição nucleófila bimolecular em fase gasosa $Cl^- + AH_3Cl$ (S_N2@A: A = C, Si, Ge, Sn, and Pb) foram teoricamente analisadas usando a teoria relativística do funcional da densidade ao nível ZORA-OLYP/TZ2P. Este estudo tem como principal objectivo explorar e compreender como a coordenada de reacção ζ e a superfície de energia potencial ao longo desta variam à medida que o centro de ataque nucleofílico varia desde o carbono aos elementos mais pesados do grupo 14. Esta análise é efectuada não só para o mecanismo mais comum de inversão de configuração (S_N2-b), mas também para o mecanismo de retenção de configuração (S_N2-f). No caso de A = C, a reacção S_N2-b apresenta uma barreira de activação. que não existe para os outros elementos do grupo 14, A = Si–Pb. Já no caso da reacção S_N2-f, esta apresenta sempre uma barreira de activação, em que a energia associada ao estado de transição é sempre mais elevada do que aquela correspondente ao mecanismo S_N2-b. No entanto, esta diferença energética entre os dois estados vai-se tornando menor à medida que se desce ao longo do grupo 14. Os efeitos relativísticos mostraram desestabilizar quer os complexos de reacção quer as espécies de transição até 10 kcal mol^{-1} (no caso de S_N2-f@Pb), apesar *de*, no entanto, não modificarem a ordem relativa das barreiras. Neste estudo, foi ainda analisada a natureza da transformação associada às reacções de retenção de configuração S_N2-f em termos de "turnstile rotation" contra o mecanismo de "Berry pseudorotation". Para compreender as tendências das barreiras de activação, as reacções modelo foram analisadas usando o modelo de "Activation Strain", em que a superfície de energia potencial $\Delta E(\zeta)$ é decomposta na energia associada à deformação dos reagentes $\Delta E_{strain}(\zeta)$ mais a interacção entre os reagentes deformados $\Delta E_{int}(\zeta)$.

$$Cl^- + H_3Ge{-}Cl \rightarrow Cl{-}GeH_3 + Cl^- \quad (3)$$

$$Cl^- + H_3Sn{-}Cl \rightarrow Cl{-}SnH_3 + Cl^- \quad (4)$$

$$Cl^- + H_3Pb{-}Cl \rightarrow Cl{-}PbH_3 + Cl^- \quad (5)$$

Likewise, frontside nucleophilic substitution (S_N2-f) at carbon has been studied much less than the regular backside pathway (S_N2-b). Yet, a number of studies on this retention-of-configuration mechanism appeared throughout the years.[3,4,13–15] Experimental support for a retention-of-configuration (or S_N2-f) mechanism was first provided in 1978 by Cayzergues et al.,[13] in a study on the reaction between lithium ethoxide and 3-chlorobut-1-ene in ethanol. Harder et al.[4] later conducted calculations which showed that for $F^- + CH_3F$, the TS of S_N2-f is 47 kcal mol^{-1} higher than the TS of regular S_N2-b, whereas for $LiF + CH_3F$, at variance, the S_N2-f pathway is more favorable than S_N2-b. In a computational study on identity S_N2 reactions of halide anions with methyl halides, Glukhovtsev et al.[14] confirmed that the frontside S_N2-f mechanism is associated with a far higher central barrier than the backside S_N2-b pathway.

Herein, we present the results of a computational study on the backside S_N2-b and frontside S_N2-f reactions at carbon and silicon [Eqs. (1)–(2)], as well as those at germanium, tin, and lead [Eqs. (3)–(5)] based on relativistic DFT calculations at zeroth-order regular approximation (ZORA)-OLYP/TZ2P as implemented in the Amsterdam Density Functional (ADF) program.[16,17] This level of theory was previously shown to agree within a few kcal mol^{-1} with highly correlated ab initio benchmarks.[18]

Our purpose is threefold. Firstly, we wish to explore and understand how the reaction coordinate ζ and potential energy surfaces (PES) along ζ vary as the center of nucleophilic attack changes from carbon to the heavier group-14 atoms. Secondly, a comparison between the more common backside reaction (S_N2-b) and the frontside pathway (S_N2-f) will be performed. The third issue is to investigate to what degree the trends are influenced by relativistic effects, especially for the most heavy group-14 congeners.

Computational Methods

General Procedure

All calculations were performed with the Amsterdam Density Functional (ADF) program developed by Baerends and others.[16,17] The molecular orbitals (MOs) were expanded in a large uncontracted set of Slater-type orbitals (STOs) containing diffuse functions, TZ2P. This basis is of triple-ζ quality and has been augmented by two sets of polarization functions: 2*p* and 3*d* on hydrogen, 3*d* and 4*f* on carbon, silicon and chlorine, 4*d* and 4*f* on germanium, 5*d* and 4*f* on tin and 5*f* and 6*d* on lead. The core shells of carbon (1*s*), silicon (1*s*2*s*2*p*), germanium (1*s*2*s*2*p*3*s*3*p*), tin (1*s*2*s*2*p*3*s*3*p*3*d*4*s*4*p*), lead (1*s*2*s*2*p*3*s*3*p*3*d*4*s*4*p*4*d*) and chlorine (1*s*2*s*2*p*) were treated by the frozen-core approximation.[16] An auxiliary set of *s*, *p*, *d*, *f* and *g* STOs was used to fit the molecular density and to represent the Coulomb and exchange potentials accurately in each SCF cycle. Relativistic effects were accounted for by using the zeroth-order regular approximation[19] (ZORA).

Energies and fully optimized geometries were computed with the OLYP[20] density functional, which involves Handy's optimized exchange (OPTX). Relativistic effects were treated using the zeroth-order regular approximation (ZORA) method.[19] This approach was previously shown to agree satisfactorily with highly correlated ab initio benchmarks.[18,21] All stationary points were confirmed by vibrational analysis:[22] for equilibrium structures all normal modes have real frequencies, whereas transition states[23] have one normal mode with one imaginary frequency. Furthermore, transition states were verified to connect the supposed reactant and product minima by carrying out intrinsic reaction coordinate (IRC) calculations.[24]

Enthalpies at 298.15 K and 1 atm (ΔH_{298}) were calculated from 0 K electronic energies (ΔE) according to [Eq. (6)], assuming an ideal gas.[25]

$$\Delta H_{298} = \Delta E + \Delta E_{\mathrm{trans},298} + \Delta E_{\mathrm{rot},298} + \Delta E_{\mathrm{vib},0} + \Delta(\Delta E_{\mathrm{vib},0})_{298} + \Delta(pV) \quad (6)$$

$\Delta E_{\mathrm{trans},298}$, $\Delta E_{\mathrm{rot},298}$, $\Delta E_{\mathrm{vib},0}$ are the differences between products and reactants in translational, rotational and zero point vibrational energy, respectively; $\Delta(\Delta E_{\mathrm{vib},0})_{298}$ is the change in the vibrational energy difference as one goes from 0 to 298.15 K. The vibrational energy corrections are based on the frequency calculations. The molar term $\Delta(pV)$ is $(\Delta n)RT$, where $\Delta n = -1$ for two reactants combining into one species. Thermal corrections for the electronic energy are neglected.

Analysis of Potential Energy Surfaces

Insight into how the activation barriers arise is obtained through Activation Strain analyses of the various S_N2 reactions.[5,26,27] The Activation Strain model[5,26,27] is a fragment approach to understanding chemical reactions, in which the height of reaction barriers is described and understood in terms of the original reactants. Thus, the potential energy surface $\Delta E(\zeta)$ is decomposed, along the reaction coordinate ζ, into the strain $\Delta E_{\mathrm{strain}}(\zeta)$ associated with deforming the individual reactants plus the actual interaction $\Delta E_{\mathrm{int}}(\zeta)$ between the deformed reactants [Eq (7); see also Figure 2]. The reaction profiles were genereated and analysed using the PyFrag program.[27]

$$\Delta E(\zeta) = \Delta E_{\mathrm{strain}}(\zeta) + \Delta E_{\mathrm{int}}(\zeta) \quad (7)$$

The strain $\Delta E_{\mathrm{strain}}(\zeta)$ is determined by the rigidity of the reactants and the extent to which groups must reorganize in a particular reaction mechanism, whereas the interaction $\Delta E_{\mathrm{int}}(\zeta)$ between the reactants depends on their electronic structure and on how they are mutually oriented as they approach each other. It is the interplay between $\Delta E_{\mathrm{strain}}(\zeta)$ and $\Delta E_{\mathrm{int}}(\zeta)$ that determines if and at which point along the ζ a barrier arises. The activation energy of a reaction $\Delta E^{\neq} = \Delta E(\zeta^{\mathrm{TS}})$ consists of the activation strain $\Delta E^{\neq}{}_{\mathrm{strain}} = \Delta E_{\mathrm{strain}}(\zeta^{\mathrm{TS}})$ plus the TS interaction $\Delta E^{\neq}{}_{\mathrm{int}} = \Delta E_{\mathrm{int}}(\zeta^{\mathrm{TS}})$:

$$\Delta E^{\neq} = \Delta E^{\neq}{}_{\mathrm{strain}} + \Delta E^{\neq}{}_{\mathrm{int}} \quad (8)$$

The interaction $\Delta E_{\mathrm{int}}(\zeta)$ between the strained reactants is further analyzed in the conceptual framework provided by the Kohn–Sham molecular orbital (KS-MO) model.[28–29] To this end, it is further decomposed into three physically meaningful terms:

$$\Delta E_{\mathrm{int}}(\zeta) = \Delta V_{\mathrm{elstat}} + \Delta E_{\mathrm{Pauli}} + \Delta E_{\mathrm{oi}} \quad (9)$$

The term $\Delta V_{\mathrm{elstat}}$ corresponds to the classical electrostatic interaction between the unperturbed charge distributions of the deformed reactants and is usually attractive. The Pauli repulsion $\Delta E_{\mathrm{Pauli}}$ comprises the destabilizing interactions between occupied orbitals and is responsible for any steric repulsion (see Ref. [28] for an exhaustive discussion). The orbital interaction ΔE_{oi} accounts for charge transfer (interaction between occupied orbitals on one moiety with unoccupied orbitals on the other, including HOMO–LUMO interactions) and polarization (empty–occupied orbital mixing on one fragment arising from the presence of another fragment).

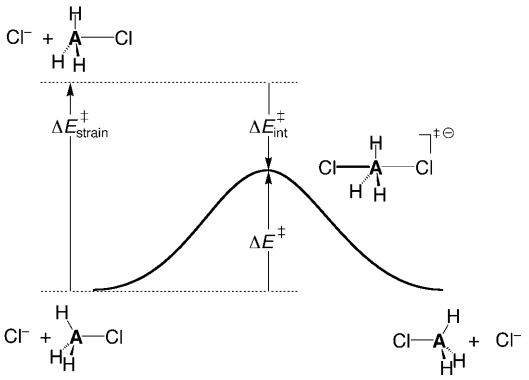

Figure 2. Illustration of the Activation Strain model in the case of a backside nucleophilic substitution of $Cl^- + AH_3Cl$ (S_N2-b@A). The activation energy, $\Delta E^{\neq}$, is decomposed into the activation strain, $\Delta E^{\neq}{}_{\mathrm{strain}}$, and the stabilizing TS interaction, $\Delta E^{\neq}{}_{\mathrm{int}}$, between the reactants in the transition state.

Results and Discussion

Backside S_N2-b: Reaction Profiles

Our ZORA-OLYP/TZ2P results for relative energies and structures of stationary points are collected in Tables 1–3 (see also Table S1 in the Supporting Information). Generic structures of stationary points are illustrated in Scheme 1. For backside nucleophilic substitution (S_N2-b), we observe the known change from a double-well PES with a central barrier and transition state **1TS-b** for the S_N2-b@C of $Cl^- + CH_3Cl$ [Eq. (1)] to a single-well PES for the S_N2-b@Si of $Cl^- + SiH_3Cl$ [Eq. (2)], in which the pentavalent transition species **2TC-b** has turned from a labile TS into a stable transition complex. This is illustrated in Figure 1. The reactant complex **1RC-b** of the S_N2-b@C reaction is bound by -9.0 kcal mol^{-1}, and it is separated from the product complex **1PC-b** by a central barrier of -8.8 kcal mol^{-1}. The S_N2-b@Si reaction features only a stable pentacoordinate TC (no TS, RC, or PC) at -24.4 kcal mol^{-1}.

Table 1. Energies (in kcal mol^{-1}) relative to reactants of stationary points occurring in backside and frontside S_N2 reactions.[a]

		Backside S_N2-b				Frontside S_N2-f					
Reaction	A	RC-b		TS-b or TC-b		TS-H		RC-f		TS-f	
1	C	−9.0	(−9.0)	−0.2	(−0.1)	[c]		[c]		40.2	(40.4)
2	Si	[b]		−24.4	(−24.4)	−6.1	(−6.2)	−9.3	(−9.4)	−6.2	(−6.3)
3	Ge	[b]		−24.3	(−24.8)	[c]		[c]		−2.1	(−3.3)
4	Sn	[b]		−32.3	(−33.7)	−14.5	(−17.5)	−16.8	(−20.0)	−15.3	(−18.6)
5	Pb	[b]		−32.3	(−36.3)	−14.3	(−21.1)	−14.5	(−23.5)	−12.9	(−22.4)

[a] Computed at ZORA-OLYP/TZ2P (nonrelativistic OLYP/TZ2P values in parentheses). [b] Nonexistent: reaction proceeds barrierless to central transition complex, TC-b. [c] Nonexistent: reaction proceeds directly from minima RC-b or TC-b to frontside transition state TS-f.

Table 2. Geometries (in Å and deg.) of stationary points occurring in backside and frontside S_N2 reactions.[a]

Species	A	A–Cl	A–Cl$^-$	A–H_a	A–H_b	Cl_a–A–H_a	H_a–A–H_b	Cl–A–Cl
AH_3Cl	C	1.792	[b]	1.090	1.090	108.4	110.5	[b]
	Si	2.066	[b]	1.489	1.489	108.9	110.0	[b]
	Ge	2.179	[b]	1.531	1.531	106.6	112.2	[b]
	Sn	2.364	[b]	1.713	1.713	105.9	112.8	[b]
	Pb	2.465	[b]	1.767	1.767	103.9	114.4	[b]
Backside S_N2-b								
1RC-b	C	1.836	3.374	1.086	1.086	108.2	110.7	180.0
1TS-b	C	2.359	2.359	1.074	1.074	90.0	120.0	180.0
2TC-b	Si	2.356	2.356	1.485	1.485	90.0	120.0	180.0
3TC-b	Ge	2.493	2.493	1.525	1.525	90.0	120.0	180.0
4TC-b	Sn	2.631	2.631	1.713	1.713	90.0	120.0	180.0
5TC-b	Pb	2.754	2.754	1.762	1.762	90.0	120.0	180.0
Frontside S_N2-f								
1TS-H	C	[c]	[c]	[c]	[c]	[c]	[c]	[c]
2TS-H	Si	2.155	2.556	1.541	1.493	102.2	96.6	110.0
3TS-H	Ge	[c]	[c]	[c]	[c]	[c]	[c]	[c]
4TS-H	Sn	2.440	2.786	1.805	1.726	98.8	96.5	104.8
5TS-H	Pb	2.538	2.924	1.878	1.776	93.6	98.8	96.2
1RC-f	C	[c]	[c]	[c]	[c]	[c]	[c]	[c]
2RC-f	Si	2.151	2.500	1.542	1.495	91.3	96.9	89.5
3RC-f	Ge	[c]	[c]	[c]	[c]	[c]	[c]	[c]
4RC-f	Sn	2.468	2.672	1.791	1.738	87.7	97.9	87.0
5RC-f	Pb	2.560	2.825	1.868	1.793	88.3	99.2	88.5
1TS-f	C	2.658	2.658	1.080	1.078	90.6	117.6	90.1
2TS-f	Si	2.293	2.293	1.497	1.523	100.8	105.6	86.9
3TS-f	Ge	2.434	2.434	1.543	1.574	99.9	108.0	85.0
4TS-f	Sn	2.564	2.564	1.735	1.768	100.7	107.7	84.7
5TS-f	Pb	2.675	2.675	1.798	1.836	99.8	109.5	84.6

[a] Computed at ZORA-OLYP/TZ2P. See Scheme 1 for definition of geometry parameters. [b] Not contained in AH_3Cl. [c] Nonexistent: reaction proceeds directly from minima RC-b or TC-b to frontside transition state TS-f.

Table 3. Energies, enthalpies, entropies and Gibbs free energies (in kcal mol^{-1} and cal mol^{-1} K^{-1}) of the transition species in backside and frontside S_N2 reactions relative to reactants.[a]

Reaction	A	ΔE	ΔH	ΔS	ΔG
Backside S_N2-b					
1	C	−0.2	−1.2	−25.1	6.3
2	Si	−24.4	−24.0	−26.1	−16.2
3	Ge	−24.3	−24.0	−24.8	−16.6
4	Sn	−32.3	−31.9	−25.2	−24.4
5	Pb	−32.3	−32.5	−24.9	−25.1
Frontside S_N2-f					
1	C	40.2	38.4	−16.9	43.4
2	Si	−6.2	−6.7	−24.8	0.6
3	Ge	−2.1	−2.9	−24.0	4.2
4	Sn	−15.3	−16.1	−24.5	−8.8
5	Pb	−12.9	−14.4	−24.8	−7.1

[a] Computed at ZORA-OLYP/TZ2P.

Here, we find that this trend further continues along the S_N2-b substitutions at the heavier central atoms germanium, tin, and lead [Eqs. (3)–(5)], which all have single-well reaction profiles with a TC at −24.3, −32.3, and −32.3 kcal mol^{-1}, respectively (see Table 1). The A–Cl bond distances of the D_{3h}-symmetric transition species are essentially equal for **1TS-b** and **2TC-b**, namely 2.36 Å, and then monotonically increases to 2.49 to 2.63 to 2.75 Å along **3TC-b**, **4TC-b**, and **5TC-b** (see Table 2). The disappearance of the central barrier from S_N2-b@C to S_N2-b@Si (and also S_N2-b@P) has previously been traced to a decrease in steric congestion in the case of the larger central atom, as well as a more favorable nucleophile–substrate interaction.[6,7]

Frontside S_N2-f: Reaction Profiles

Frontside nucleophilic substitution (S_N2-f) proceeds, at variance with backside S_N2-b, in all cases via a central barrier and a C_s-symmetric pentavalent TS that is significantly higher in energy than the corresponding transition species for backside substitution (S_N2-b). Thus, the TS for the S_N2-f substitutions is at 40.2 (C), −6.2 (Si), −2.1 (Ge), −15.3 (Sn), and −12.9 kcal mol^{-1} (Pb) relative to the reactants, which has to be compared with the corresponding transition species of the backside S_N2-b pathway, which are at −0.2 (C), −24.4 (Si), −24.3 (Ge), −32.3 (Sn), and −32.3 kcal mol^{-1} (Pb) (see Table 1). The frontside S_N2-f pathway can, in all cases, be characterized by a double-well PES, but the nature of the minima may differ between the various model reaction systems.

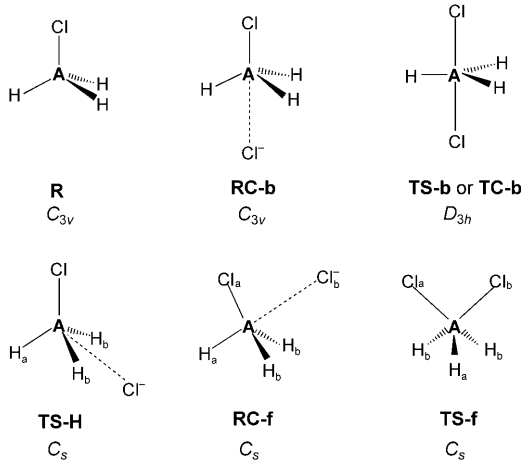

Scheme 1. Structures of stationary points for backside S_N2-b and frontside S_N2-f.

The frontside S_N2-f@C reaction of $Cl^- + CH_3Cl$ proceeds via the same reactant and product complexes **1RC-b** and **1PC-b** as the backside S_N2-b@C pathway (see Scheme 2).

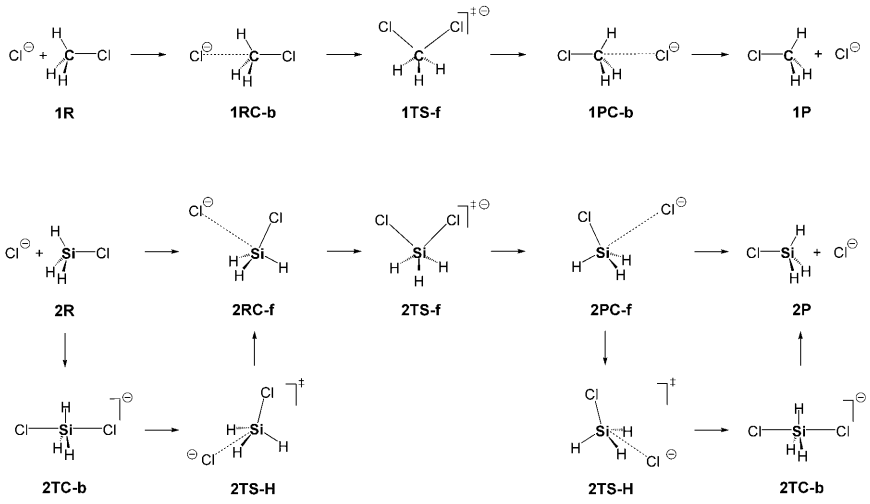

Scheme 2. Stationary points along frontside S_N2-f at carbon and silicon.

Separate frontside reactant and product complexes do not exist for this model system. The minima **1RC-b** and **1PC-b** on the double-well PES are now interconverted via the C_s-symmetric transition state, **1TS-f** (Scheme 2), at 40.2 kcal mol^{-1} (see Table 1). This corresponds to a central barrier of 49.2 kcal mol^{-1}. In **1TS-f**, the nucleophile and leaving group are direct neighbors that bind to carbon by the two equivalent C–Cl bonds of 2.66 Å (see Scheme 1 and Table 2).

The frontside S_N2-f@Si reaction of $Cl^- + SiH_3Cl$ may proceed via characteristic frontside reactant and product complexes **2RC-f** and **2PC-f** that are bound by −9.3 kcal mol^{-1} relative to separate reactants or products (see Scheme 2 and Table 1). These minima on the double-well PES are interconverted via the C_s-symmetric transition state, **2TS-f** (Scheme 2), at −6.2 kcal mol^{-1} (see Table 1), which corresponds to a central barrier of 3.1 kcal mol^{-1}. In **2TS-f**, the nucleophile and leaving group are direct neighbors that bind to silicon via two equivalent Si–Cl bonds of 2.29 Å (see Scheme 1 and Table 2). Alternatively, the reaction may also proceed by prior association of the reactants in the stable transition complex **2TC-b** of the backside pathway at −24.4 kcal mol^{-1}. From here, instead of following the S_N2-b pathway, the frontside reactant complex **2RC-f** is obtained through rearrangement via transition state **2TS-H**, at −6.1 kcal mol^{-1}, in which the Cl^- nucleophile is migrating on the bisector, in between two Si–H bonds, towards the frontside (see Scheme 2 and Table 1). The corresponding process can occur in the product complex. Additionally, the leaving group may undergo an equivalent migration, which represents a shortcut from **2TC-b** to **2PC-f** not shown in Scheme 2.

The frontside S_N2-f substitutions at the heavier group-14 atoms Ge, Sn, and Pb show similar reaction profiles and stationary points as that for S_N2@Si, with one exception. In the case of the S_N2-f@Ge reaction of $Cl^- + GeH_3Cl$, the intrinsic reaction coordinate (IRC) leads from the frontside **3TS-f** directly to the backside transition complex **3TC-b**. No stable frontside reactant or product complexes, and no transition state of the type TS-H exist on the PES of this reaction pathway.

The trends found on the PESes, that is, in terms of relative energies, are hardly affected by zero-point vibrational and thermal effects as well as entropy effects computed at 298 K (see Table 3). Thus, enthalpies ΔH_{298} of transition species (TS or TC) relative to reactants differ by about 2 kcal mol^{-1} or less from the corresponding energies. The decreased density of states in the more tightly bound transition species leads consistently to a reduction in entropy ΔS_{298} of some −24 to −26 cal mol^{-1}K^{-1}, which translates into a destabilization of the Gibbs free energies ΔG_{298} (as compared to the enthalpies ΔH_{298}) of 6 to 8 kcal mol^{-1} (see Table 3). A somewhat smaller, negative activation entropy ΔS_{298} is obtained for frontside S_N2-f substitution at carbon, only −16.9 cal mol^{-1}K^{-1}, which corresponds to a slight destabilization of 3 kcal mol^{-1} of the activation Gibbs free energy ΔG_{298} (as compared to the activation enthalpy ΔH_{298}).

Frontside S_N2-f: Berry Pseudorotation and/or Turnstile Rotation?

The backside S_N2-b process leads to inversion of configuration of the AH_3 moiety whereas the frontside S_N2-f pathway goes with retention of configuration. However, whereas the overall transformation of the backside pathway is easily envisaged as an "inverting umbrella" the situation is, at first sight, somewhat less clear in the case of the frontside substitution. The question is, in particular, how and to which position the three H atoms move while the nucleophile Cl and leaving group Cl exchange their axial and equatorial position from **RC-f** to **PC-f**.

Ligand rearrangements in pentavalent silicon compounds have been described, among others, in terms of the Berry Pseudorotation[30] and the Turnstile Rotation[31] mechanisms. These two mechanisms are illustrated in Scheme 3 for our frontside S_N2-f process. It will become clear in a moment that Berry Pseudorotation and Turnstile Rotation are two ways of looking at one and the same geometrical transformation. In the Berry Pseudorotation mechanism, the axial Cl^4 (nucleophile) and H^3 bent to the right, away from the equatorial H^1, and become themselves equatorial while the equatorial Cl^5 (leaving group) and H^2 bent to the left, to-

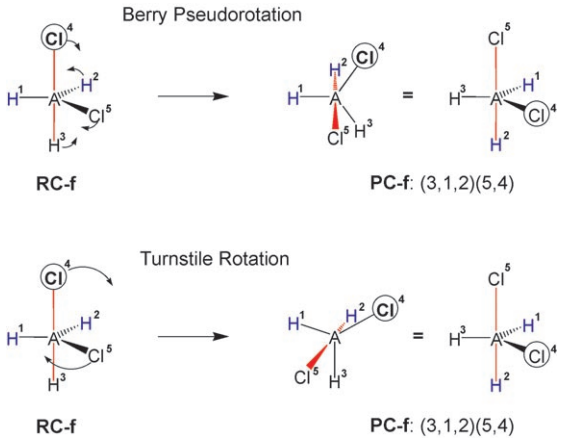

Scheme 3. Berry-Pseudorotation and Turnstile-Rotation Mechanisms (red: axial bonds).

wards the equatorial H^1, which is standing still (Scheme 3, upper). The result is a permutation of positions in the trigonal bipyramid indicated as (1,2,3)(4,5)→(3,1,2)(5,4), that is, H^3 to H^1, H^1 to H^2, H^2 to H^3, and Cl^5 to Cl^4, Cl^4 to Cl^5, indicated as (3,1,2)(5,4).

In the Turnstile Rotation mechanism, the axial Cl^4 (nucleophile) and the equatorial Cl^5 (leaving group) are conceived as a pair that rotates with respect to the AH_3 moiety, such that Cl^4 adopts an equatorial position in between H^1 and H^3 (which in the course also changes from axial to equatorial!), and Cl^5 adopts an axial position opposite to H^2 (which thus, also changes from equatorial to axial!). Note that the result is again a (3,1,2)(5,4) permutation of positions, identical to the result of the Berry Pseudorotation.

Next, we have examined in detail, for all five reaction systems, the nature of the motions in the frontside S_N2-f transition state and along the IRC that leads away from this TS. The motions appear in all five transition states (i.e., for A = C, Si, Ge, Sn, and Pb) as a rotation between the pair of Cl^4 and Cl^5 relative to the trio of H^1, H^2, and H^3 as shown in Scheme 4. In the case of A = Si, Sn, and Pb, this corresponds to the (3,1,2)(5,4) permutation of positions, discussed previously, as we go from **RC-f** to **PC-f**. In the perspective shown in Scheme 4, this appears as a relative rotation over 50°. The reduced mass associated with this normal mode is approximately equal to that of the three hydrogens (as they are much lighter than the two chlorines), and a visualization of the normal mode and the IRC therefore shows an AH_3 group rotating with respect to the two Cl atoms that are practically standing still.

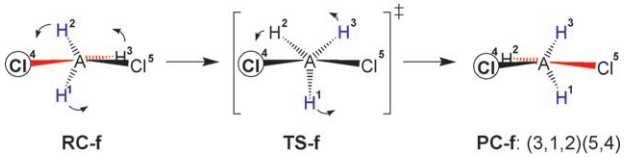

Scheme 4. IRC of all frontside S_N2-f substitutions (red: axial bonds).

The fact that the transition vector and the IRC associated with the frontside S_N2-f substitutions appears as a rotation, makes it natural to designate this process as a Turnstile Rotation. However, we stress that this is not really different from the Berry Pseudorotation, it is just a different way of expressing the overall transformation in terms of partial motions. In fact, if one considers the Berry Pseudorotation in Scheme 3 more carefully, one can recognize that the simultaneous bending of the two A–Cl bonds together, generates a rotational motion of Cl^4 and Cl^5 relative to the AH_3 fragment.

Backside S_N2-b: Activation Strain Analyses

Next, we examine why S_N2 central barriers decrease as the central atom descends in group 14, and why they are higher for frontside S_N2-f than backside S_N2-b. To this end, we have carried out Activation Strain analyses (see Eqs. 7–9)[5,26] of the reaction potential energy surfaces (PES) along the IRC projected onto the nucleophile–central atom distance (Nu–A). Because there is no central barrier and no TS in the backside S_N2-b reactions of the heavier group-14 central atoms, the IRC is modeled for this pathway by a linear transit, in which the Nu–A distance and the central atom–leaving group (A–L) distance run synchronously in 20 steps from their value in the D_{3h}-symmetric transition species to that in the RC-b (for A = C), or to a geometry that closely resembles the separate reactants defined as Nu–A = 6 Å and A–L = equilibrium value in isolated substrate (for A = Si, Ge, Sn, Pb). For the S_N2-b reaction of $Cl^- + CH_3Cl$, we have verified that this yields essentially the same reaction profiles as the one based on a regular IRC. The results of the Activation Strain analyses are collected in Figure 3, in which the reaction coordinate is the nucleophile–central atom distance Cl^-–A relative to the transition species, at which it is set to 0. Note that in the graphs of Figure 3 the reaction proceeds from the right to the left.

Figure 3a shows the reaction profiles of our backside and frontside substitutions (for numerical data, see Table 1). The disappearance of the central barrier in the backside S_N2-b reaction from A = C to Si is because of both a reduced strain ΔE_{strain} and a more stabilizing nucleophile–substrate interaction ΔE_{int} (compare black and red curves in Figure 3b, left). The origin of this decrease in strain for $Cl^- + SiH_3Cl$ has been recently traced to the reduced steric congestion and steric (Pauli) repulsion between the five substituents in the D_{3h}-symmetric pentavalent transition species as the central atom becomes larger from C to Si.[6,7] The stronger interaction in the latter case arises from the better nucleophile–substrate $\langle 3p\,|\,\sigma^*_{A-Cl}\rangle$ overlap if the relatively diffuse Cl^--3*p* AO approaches the more extended silicon-3*p* lobe of SiH_3Cl σ^*_{Si-Cl} (0.29 in **2TC-b**), than if it approaches the compact 2*p* lobe in the CH_3Cl σ^*_{C-Cl} LUMO (0.21 in **1TS-b**, not shown in the tables). The contour plots in Figure 4 provide a graphical representation of the shape of the substrate, σ^*_{A-Cl} LUMO, and how this obtains a more

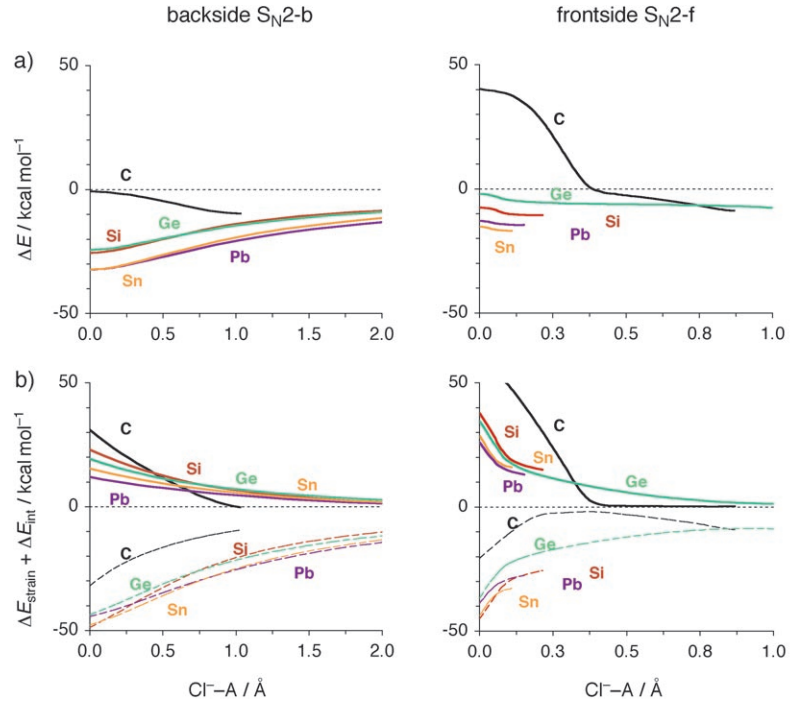

Figure 3. Analysis of backside and frontside S_N2 reactions of $Cl^- + AH_3Cl$ with A = C, Si, Ge, Sn, Pb along the intrinsic reaction coordinate projected onto the Cl^-–A (i.e., Nu–A) distance relative to the transition species, at which Cl^-–A = 0: (a) potential energy surface ΔE; (b) decomposition $\Delta E = \Delta E_{strain} + \Delta E_{int}$, indicated with plain and dashed curves, respectively.

extended backside lobe if we go from A = C to Si (see also Ref. [32]).

Our analyses show that the trend of decreasing strain from $Cl^- + CH_3Cl$ to $Cl^- + SiH_3Cl$ continues also along the backside S_N2-b substitutions at the heavier group-14 atoms. Thus, the ΔE_{strain} curves in Figure 3b, left, become less and less destabilizing as the size of the central atom increases along A = C, Si, Ge, Sn, and Pb, and the steric congestion decreases. The nucleophile–substrate interaction is furthermore consistently more stabilizing for S_N2-b substitution with the heavier group-14 atoms than with carbon because of the better HOMO–LUMO overlap and thus orbital interactions and a stronger electrostatic attraction [see Eq. (9)] with the more electropositive central atom,[32] in particular, in the case of A = Pb (not shown in the tables).

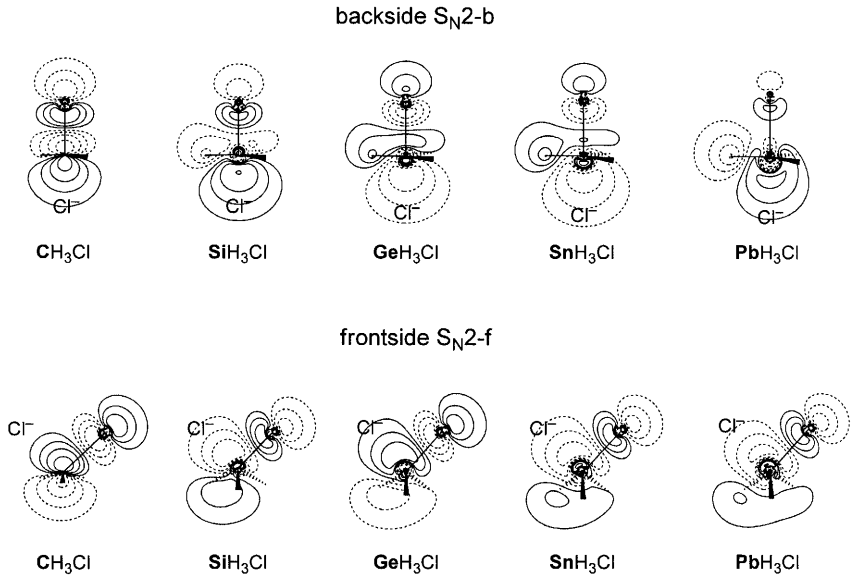

Figure 4. Contour plots of the $\sigma^*_{A\text{-}Cl}$ acceptor orbital of AH_3Cl fragments (see wire frames) in backside S_N2-b and frontside S_N2-f transition species, computed at ZORA-OLYP/TZ2P (scan values: 0.0, ±0.02, ±0.05, ±0.1, ±0.2, ±0.5; solid and dashed contours refer to positive and negative values). For each AH_3Cl-$\sigma^*_{A\text{-}Cl}$ orbital, the position of the nucleophile Cl^- in the corresponding transition species is indicated.

Frontside S_N2-f: Activation Strain Analyses

The destabilization of the frontside S_N2-f transition states compared to the corresponding backside S_N2-b transition species (TS or TC) is mainly the result of increased activation strain as can be seen from a comparison of the strain curves ΔE_{strain} in the left and right panels of Figure 3b. This is so especially for S_N2-f@C, for which the ΔE_{strain} curve runs off the scale: for comparison, $\Delta E^{\neq}_{strain}$ amounts to 31.8 and 60.8 kcal mol^{-1} in **1TS-b** and **1TS-f**, respectively (not shown in tables). Additionally, the nucleophile–substrate interaction ΔE_{int} is weakened from backside to frontside substitution (compare again left and right panels of Figure 3b). This effect is however, significantly smaller than the destabilization of the activation strain. For example, $\Delta E^{\neq}_{int}$ amounts to −32.0 and −20.6 kcal mol^{-1} in **1TS-b** and **1TS-f**, respectively (not shown in tables).

The weakening of ΔE_{int} originates from the poor bond overlap in the frontside orientation between the Cl^--3*p* AOs and the AH_3Cl-$\sigma^*_{A\text{-}Cl}$ acceptor orbital. Thus, the $\langle 3p | \sigma^*_{A\text{-}Cl} \rangle$ over-

lap in the frontside TS-f varies from 0.10 to 0.26 to 0.23 to 0.24 to 0.19 along A = C, Si, Ge, Sn, and Pb (not shown in tables).[33] This has to be compared with the larger overlap values in the corresponding backside transition species, which vary from 0.21 to 0.29 to 0.27 to 0.28 to 0.22 (not shown in tables). The reason for this effect is the cancellation of overlap as the Cl^--3*p* AO approaches the $\sigma^*_{A\text{-}Cl}$-acceptor orbital in the frontside orientation at its nodal surface (see Scheme 5). Such cancellation of overlap does not

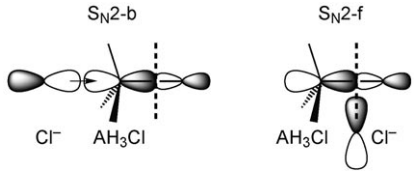

Scheme 5. Overlap between Cl^--3*p* HOMO and AH_3Cl-$\sigma^*_{A\text{-}Cl}$ LUMO in S_N2-b and S_N2-f.

occur when the Cl^--3*p* AO approaches the backside lobe of the $\sigma^*_{A\text{-}Cl}$-acceptor orbital (see Scheme 5). The cancellation of overlap is the largest for A = C and becomes less pronounced for the heavier group-14 central atoms. The reason is the increasing amplitude of the central atom's n*p* AO in $\sigma^*_{A\text{-}Cl}$ as this atom becomes more electropositive (see Figure 4). This overlap argument has been proposed on qualitative grounds by Anh and Minot[34] and is here quantitatively confirmed for general S_N2 reactions.

Yet, interestingly, it is not reduced bond overlap but an increased strain that is the dominant factor causing the higher frontside S_N2-f barriers, as pointed out above (see also Figure 3b). This can be traced to the fact that in the frontside substitution, two large substituents, that is the nucleophile and the leaving group, must be accommodated in the pentavalent transition state. This unfavorable situation causes a slightly larger deformation in the case of the heavier group-14 atoms (see Table 2). But in the case of the sterically congested carbon, it causes a more significant and energetically quite unfavorable deformation (see Table 2). This is aggravated by the fact that the CH_3 moiety is relatively rigid and gives in much less to the steric pressure of the (unfavorably placed) fifth substituent than the C–Cl (leaving group) bond. The result is a strongly expanded C–Cl distance of 2.658 Å, which has to be compared with the much shorter C–Cl bond of 2.359 Å in **1TS-b** or the Si–Cl bond of 2.293 Å in **2TS-f** (see Table 2). This more weakly bound character of the **1TS-f** is associated with a higher density of states, which is reflected by the less negative activation entropy ΔS_{298} for this reaction mechanism mentioned previously (see also Table 3).

Relativistic Effects

We have assessed the importance of taking relativistic effects into account by comparing our relativistic ZORA-OLYP/TZ2P reaction profiles with nonrelativistic OLYP/TZ2P results. The latter are also shown in Table 1 in parentheses. The main trends for the $Cl^- + AH_3Cl$ substitution reactions are preserved if relativity is neglected, that is, decreasing barriers as the central atom descends in group 14, and higher frontside than backside barriers.

Absolute values of barriers can, however, be significantly affected by relativity, which destabilizes the stationary points relative to reactants. For the carbon-, silicon-, and germanium-containing systems, the relativistic effects are in the range of negligible to small, up to approximately 1 kcal mol^{-1} for A = Ge. However, in the case of A = Sn and Pb, the frontside S_N2-f transition state is destabilized by about 3 and 10 kcal mol^{-1}, respectively. Note that relativistic destabilization is more pronounced for the frontside than for the backside transition states, making the former even less viable than they already are.

The origin of the relativistic destabilization has been traced to the relativistic contraction and energy lowering of the central atom-n*p* AOs. This causes their amplitude in the antibonding-$\sigma^*_{A\text{-}Cl}$ acceptor orbital to become smaller, which in turn leads to a smaller overlap and less stabilizing donor–acceptor orbital interaction with the nucleophile Cl^--3*p* HOMO. In the case of $Cl^- + PbH_3Cl$, for example, switching on relativity causes the $\langle 3p_z | \sigma^*_{Pb\text{-}Cl} \rangle$ overlap in **5TS-b** to decrease from 0.272 to 0.216, which goes with a weakening of the nucleophile-substrate interaction, ΔE_{int}, from −50.6 to −44.3 kcal mol^{-1} (not shown in the tables).

Conclusions

Activation Strain analyses show that the central barrier for backside nucleophilic substitution (S_N2-b) of $Cl^- + AH_3Cl$ disappears as the central atom A goes from carbon to silicon, and the heavier group-14 atoms (up till lead). This is because the steric congestion (and repulsion) decreases for the larger central atoms, and the orbital interactions become more stabilizing resulting from a better overlap between the chloride-3p_z HOMO and the substrate-$\sigma^*_{A\text{-}Cl}$ LUMO, which obtains an increasingly extended amplitude on an even more electropositive atom A.

Furthermore, frontside nucleophilic substitution (S_N2-f) proceeds in all cases via a central barrier associated with a C_s-symmetric pentavalent TS, that is significantly higher in energy than the corresponding transition species for backside substitution (S_N2-b). One reason is the less efficient ⟨chloride HOMO | substrate LUMO⟩ overlap for S_N2-f that has been noted previously.[34]

Interestingly, however, the main reason for the higher barrier for frontside substitution is the increased steric repulsion between nucleophile and leaving group, which are adjacent in the TS for frontside S_N2-f while they are on opposite sides of the trigonal bipyramidal transition structure for backside S_N2-b.

Acknowledgements

We thank the Netherlands Organization for Scientific Research (NWO-CW) for financial support.

[1] M. B. Smith, J. March, *March's Advanced Organic Chemistry: Reactions, Mechanisms, and Structure*, Wiley, New York, **2007**; C. Ingold, *Structure and Mechanism in Organic Chemistry*, Cornell University, Ithaca, NY, **1969**; T. H. Lowry, K. S. Richardson, *Mechanism and Theory in Organic Chemistry*, Harper and Row, New York, **1987**; F. A. Carey, R. J. Sundberg, *Advanced Organic Chemistry, Part A*, Springer, New York, **2007**.

[2] G. Vayner, K. N. Houk, W. L. Jorgensen, J. I. Brauman, *J. Am. Chem. Soc.* **2004**, *126*, 9054; S. Gronert, *Acc. Chem. Res.* **2003**, *36*, 848; J. K. Laerdahl, E. Uggerud, *Int. J. Mass Spectrom.* **2002**, *214*, 277; M. L. Chabinyc, S. L. Craig, C. K. Regan, J. I. Brauman, *Science* **1998**, *279*, 1882; S. S. Shaik, H. B. Schlegel, S. Wolfe, *Theoretical Aspects of Physical Organic Chemistry: The S_N2 Mechanism*, Wiley, New York, **1992**; W. N. Olmstead, J. I. Brauman, *J. Am. Chem. Soc.* **1977**, *99*, 4219; P. Botschwina, *Theor. Chem. Acc.* **1998**, *99*, 426; J. Chandrasekhar, S. F. Smith, W. L. Jorgensen, *J. Am. Chem. Soc.* **1985**, *107*, 154; I. Lee, C. K. Kim, C. K. Sohn, H. G. Li, H. W. Lee, *J. Phys. Chem. A* **2002**, *106*, 1081; N. M. M. Nibbering, *Acc. Chem. Res.* **1990**, *23*, 279; C. H. DePuy, S. Gronert, A. Mullin, V. M. Bierbaum, *J. Am. Chem. Soc.* **1990**, *112*, 8650; M. A. van Bochove, M. Swart, F. M. Bickelhaupt, *ChemPhysChem* **2007**, *8*, 2452; R. D. Bach, O. Dmitrenko, C. Thorpe, *J. Org. Chem.* **2008**, *73*, 12; M. A. van Bochove, F. M. Bickelhaupt, *Eur. J. Org. Chem.* **2008**, 649; M. N. Glukhovtsev, A. Pross, L. Radom, *J. Am. Chem. Soc.* **1995**, *117*, 2024; S. H. Norton, S. M. Bachrach, J. M. Hayes, *J. Org. Chem.* **2005**, *70*, 5896; S. M. Bachrach, A. Pereverzev, *Org. Biomol. Chem. Org. Biom. Chem.* **2005**, *3*, 2095.

[3] L. Deng, V. Branchadell, T. Ziegler, *J. Am. Chem. Soc.* **1994**, *116*, 10645.

[4] S. Harder, A. Streitwieser, J. T. Petty, P. v. R. Schleyer, *J. Am. Chem. Soc.* **1995**, *117*, 3253.

[5] F. M. Bickelhaupt, *J. Comput. Chem.* **1999**, *20*, 114.

[6] A. P. Bento, F. M. Bickelhaupt, *J. Org. Chem.* **2007**, *72*, 2201; M. A. van Bochove, M. Swart, F. M. Bickelhaupt, *J. Am. Chem. Soc.* **2006**, *128*, 10738.

[7] S. C. A. H. Pierrefixe, C. Fonseca Guerra, F. M. Bickelhaupt, *Chem. Eur. J.* **2008**, *14*, 819.

[8] A. T. P. Carvalho, M. Swart, J. N. P. van Stralen, P. A. Fernandes, M. J. Ramos, F. M. Bickelhaupt, *J. Phys. Chem. B* **2008**, *112*, 2511.

[9] C. Elschenbroich, *Organometallics* Wiley-VCH, Weinheim, **2006**; L. H. Sommer, *Stereochemistry, Mechanism and Silicon*, McGraw Hill, New York, **1965**; R. R. Holmes, *Chem. Rev.* **1990**, *90*, 17; R. Damrauer, J. A. Hankin, *Chem. Rev.* **1995**, *95*, 1137; M. J. S. Dewar, E. Healy, *Organometallics* **1982**, *1*, 1705; J. C. Sheldon, R. N. Hayes, J. H. Bowie, *J. Am. Chem. Soc.* **1984**, *106*, 7711; R. Damrauer, L. W. Burggraf, L. P. Davis, M. S. Gordon, *J. Am. Chem. Soc.* **1988**, *110*, 6601; T. L. Windus, M. S. Gordon, L. P. Davis, L. W. Burggraf, *J. Am. Chem. Soc.* **1994**, *116*, 3568; S. Gronert, R. Glaser, A. Streitwieser, *J. Am. Chem. Soc.* **1989**, *111*, 3111; C. H. DePuy, V. M. Bierbaum, L. A. Flippin, J. J. Grabowski, G. K. King, R. J. Schmitt, S. A. Sullivan, *J. Am. Chem. Soc.* **1980**, *102*, 5012; F. Méndez, M. d. L. Romero, J. L. Gazquez, *J. Chem. Sci.* **2005**, *117*, 525; R. L. Hilderbrandt, G. D. Homer, P. Boudjouk, *J. Am. Chem. Soc.* **1976**, *98*, 7476; Z. Shi, R. J. Boyd, *J. Phys. Chem.* **1991**, *95*, 4698; J. H. Bowie, *Acc. Chem. Res.* **1980**, *13*, 76; H. van der Wel, N. M. M. Nibbering, J. C. Sheldon, R. N. Hayes, J. H. Bowie, *J. Am. Chem. Soc.* **1987**, *109*, 5823; E. P. A. Couzijn, A. W. Ehlers, M. Schakel, K. Lammertsma, *J. Am. Chem. Soc.* **2006**, *128*, 13634.

[10] C. Hao, J. D. Kaspar, C. E. Check, K. C. Lobring, T. M. Gilbert, L. S. Sunderlin, *J. Phys. Chem. A* **2005**, *109*, 2026.

[11] V. A. Benin, J. C. Martin, M. R. Willcott, *Tetrahedron* **1997**, *53*, 10133.

[12] R. E. Allan, M. A. Beswick, M. K. Davies, P. R. Raithby, A. Steiner, D. S. Wright, *J. Organomet. Chem.* **1998**, *550*, 71.

[13] P. Cayzergues, C. Georgoulis, G. Ville, *J. Chem. Res. Synop.* **1978**, 325.

[14] M. N. Glukhovtsev, A. Pross, H. B. Schlegel, R. D. Bach, L. Radom, *J. Am. Chem. Soc.* **1996**, *118*, 11258.

[15] E. Uggerud, L. Bache-Andreassen, *Chem. Eur. J.* **1999**, *5*, 1917.

[16] G. te Velde, F. M. Bickelhaupt, E. J. Baerends, C. Fonseca Guerra, S. J. A. van Gisbergen, J. G. Snijders, T. Ziegler, *J. Comput. Chem.* **2001**, *22*, 931; E. J. Baerends, D. E. Ellis, P. Ros, *Chem. Phys.* **1973**, *2*, 41.

[17] C. Fonseca Guerra, J. G. Snijders, G. te Velde, E. J. Baerends, *Theor. Chem. Acc.* **1998**, *99*, 391; *Computer code ADF 2006.01*: E. J. Baerends, J. Autschbach, A. Bérces, J. A. Berger, F. M. Bickelhaupt, C. Bo, P. L. de Boeij, P. M. Boerrigter, L. Cavallo, D. P. Chong, L. Deng, R. M. Dickson, D. E. Ellis, M. van Faassen, L. Fan, T. H. Fischer, C. Fonseca Guerra, S. J. A. van Gisbergen, J. A. Groeneveld, O. V. Gritsenko, M. Grüning, F. E. Harris, P. van den Hoek, C. R. Jacob, H. Jacobsen, L. Jensen, E. S. Kadantsev, G. van Kessel, R. Klooster, F. Kootstra, E. van Lenthe, D. A. McCormack, A. Michalak, J. Neugebauer, V. P. Nicu, V. P. Osinga, S. Patchkovskii, P. H. T. Philipsen, D. Post, C. C. Pye, W. Ravenek, P. Romaniello, P. Ros, P. R. T. Schipper, G. Schreckenbach, J. Snijders, M. Solà, M. Swart, D. Swerhone, G. te Velde, P. Vernooijs, L. Versluis, L. Visscher, O. Visser, F. Wang, T. A. Wesolowski, E. M. van Wezenbeek, G. Wiesenekker, S. K. Wolff, T. K. Woo, A. L. Yakovlev, T. Ziegler, SCM, Amsterdam, The Netherlands.

[18] A. P. Bento, M. Solà, F. M. Bickelhaupt, *J. Comput. Chem.* **2005**, *26*, 1497; G. T. de Jong, M. Solà, L. Visscher, F. M. Bickelhaupt, *J. Chem. Phys.* **2004**, *121*, 9982; G. T. de Jong, D. P. Geerke, A. Diefenbach, F. M. Bickelhaupt, *Chem. Phys.* **2005**, *313*, 261; G. T. de Jong, D. P. Geerke, A. Diefenbach, M. Solà, F. M. Bickelhaupt, *J. Comput. Chem.* **2005**, *26*, 1006; G. T. de Jong, F. M. Bickelhaupt, *J. Phys. Chem. A* **2005**, *109*, 9685; G. T. de Jong, F. M. Bickelhaupt, *J. Chem. Theory Comput.* **2006**, *2*, 322.

[19] E. van Lenthe, E. J. Baerends, J. G. Snijders, *J. Chem. Phys.* **1994**, *101*, 9783.

[20] N. C. Handy, A. J. Cohen, *Mol. Phys.* **2001**, *99*, 403; C. Lee, W. Yang, R. G. Parr, *Phys. Rev. B* **1988**, *37*, 785.

[21] M. Swart, A. W. Ehlers, K. Lammertsma, *Mol. Phys.* **2004**, *102*, 2467; J. Baker, P. Pulay, *J. Chem. Phys.* **2002**, *117*, 1441; X. Xu, W. A. Goddard III, *J. Phys. Chem. A* **2004**, *108*, 8495; J. M. Gonzales, W. D. Allen, H. F. Schaefer III, *J. Phys. Chem. A* **2005**, *109*, 10613; M. Grüning, O. V. Gritsenko, E. J. Baerends, *J. Phys. Chem. A* **2004**, *108*, 4459.

[22] L. Fan, L. Versluis, T. Ziegler, E. J. Baerends, W. Ravenek, *Int. J. Quantum Chem. Quantum Chem. Symp.* **1988**, *34*, 173.

[23] L. Fan, T. Ziegler, *J. Chem. Phys.* **1990**, *92*, 3645.

[24] K. Fukui, *Acc. Chem. Res.* **1981**, *14*, 363.

[25] P. W. Atkins, *Physical Chemistry*, Oxford University, Oxford, **1998**.

[26] A. Diefenbach, G. T. de Jong, F. M. Bickelhaupt, *J. Chem. Theory Comput.* **2005**, *1*, 286; A. Diefenbach, F. M. Bickelhaupt, *J. Chem. Phys.* **2001**, *115*, 4030; G. T. de Jong, F. M. Bickelhaupt, *ChemPhysChem* **2007**, *8*, 1170.

[27] W. J. van Zeist, C. Fonseca Guerra, F. M. Bickelhaupt, *J. Comput. Chem.* **2008**, *29*, 312.

[28] For our quantitative MO approach see: F. M. Bickelhaupt, E. J. Baerends in *Reviews in Computational Chemistry*, *Vol. 15* (Eds.: K. B. Lipkowitz, D. B. Boyd) Wiley-VCH, New York, **2000**, p. 1; E. J. Baerends, O. V. Gritsenko, *J. Phys. Chem. A* **1997**, *101*, 5383; For an overview of qualitative MO theory, see: R. Hoffmann, *Angew. Chem.* **1982**, *94*, 725; *Angew. Chem. Int. Ed. Engl.* **1982**, *21*, 711.

[29] F. M. Bickelhaupt, N. M. M. Nibbering, E. M. van Wezenbeek, E. J. Baerends, *J. Phys. Chem.* **1992**, *96*, 4864; F. M. Bickelhaupt, A. Diefenbach, S. P. de Visser, L. J. de Koning, N. M. M. Nibbering, *J. Phys. Chem. A* **1998**, *102*, 9549; T. Ziegler, A. Rauk, *Inorg. Chem.* **1979**, *18*, 1558; T. Ziegler, A. Rauk, *Theor. Chim. Acta* **1977**, *46*, 1; T. Ziegler, A. Rauk, *Inorg. Chem.* **1979**, *18*, 1755.

[30] R. S. Berry, *J. Chem. Phys.* **1960**, *32*, 933; K. Mislow, *Acc. Chem. Res.* **1970**, *3*, 321.
[31] I. Ugi, D. Marquarding, H. Klusacek, P. Gillespie, *Acc. Chem. Res.* **1971**, *4*, 288; P. Gillespie, P. Hoffman, H. Klusacek, D. Marquarding, S. Pfohl, F. Ramirez, E. A. Tsolis, I. Ugi, *Angew. Chem.* **1971**, *83*, 691; *Angew. Chem. Int. Ed. Engl.* **1971**, *10*, 687.
[32] F. M. Bickelhaupt, T. Ziegler, P. v. R. Schleyer, *Organometallics* **1996**, *15*, 1477.
[33] Computed as $\langle 3p\,|\,\sigma^*_{A\text{-}Cl}\rangle = [(\langle 3p_x\,|\,\sigma^*_{A\text{-}Cl}\rangle)^2 + (\langle 3p_y\,|\,\sigma^*_{A\text{-}Cl}\rangle)^2 + (\langle 3p_z\,|\,\sigma^*_{A\text{-}Cl}\rangle)^2]^{1/2}$.
[34] N. T. Anh, C. Minot, *J. Am. Chem. Soc.* **1980**, *102*, 103.

Received: February 27, 2008
Published online: August 19, 2008

